Heterostructured Lepidocrocite Titanate-Carbon Nanosheets for Electrochemical Applications

Journal:	*ACS Applied Nano Materials*
Manuscript ID	an-2021-03449z.R2
Manuscript Type:	Article
Date Submitted by the Author:	06-Dec-2021
Complete List of Authors:	Barim, Gözde; Lawrence Berkeley National Laboratory, Energy Storage & Distributed Resources Dhall, Rohan; Lawrence Berkeley National Laboratory, National Center for Electron Microscopy Arca, Elisabetta; Newcastle University Kuykendall, Tevye; E O Lawrence Berkeley National Laboratory, Materials Sciences Yin, Wei; Lawrence Berkeley National Laboratory, Energy Storage & Distributed Resources Takeuchi, Kenneth; Stony Brook University, Takeuchi, Esther; Stony Brook University, Materials Science and Engineering Marschilok, Amy; Stony Brook University, Materials Science and Engineering Doeff, Marca; E O Lawrence Berkeley National Laboratory, Energy Storage and Distributed Resources Division

Heterostructured Lepidocrocite Titanate-Carbon Nanosheets for Electrochemical Applications

Gözde Barim[1], Rohan Dhall[2], Elisabetta Arca[1], Tevye R. Kuykendall[3], Wei Yin[1], Kenneth J. Takeuchi[4,5], Esther S. Takeuchi[4,5,6], Amy C. Marschilok[4,5,6], Marca M. Doeff[1,*]

1. Energy Storage & Distributed Resources Division, Lawrence Berkeley National Laboratory, Berkeley, CA, 94720, USA.
2. National Center for Electron Microscopy, Molecular Foundry, Lawrence Berkeley National Laboratory, CA, 94720, USA.
3. Molecular Foundry, Lawrence Berkeley National Laboratory, CA, 94720, USA.
4. Department of Chemistry, Stony Brook University, Stony Brook, NY, 11794, USA.
5. Department of Materials Science and Chemical Engineering, Stony Brook University, Stony Brook, NY, 11794, USA.
6. Energy and Photon Sciences Directorate, Brookhaven National Laboratory, Upton, NY, 11973, USA.

*E-mail: mmdoeff@lbl.gov

Abstract

Lepidocrocite-type titanates that reversibly intercalate sodium ions at low potentials (~0.6 V vs. Na/Na^+) are promising anode candidates for sodium ion batteries. However, large amounts of carbon additives are often used to improve their electrical conductivity and overcome poor cycling performance in the electrode composites. To ameliorate electronic transport issues of lepidocrocite titanate ($K_{0.8}Ti_{1.73}Li_{0.27}O_4$, KTL) in sodium ion batteries, we have designed and synthesized heterostructures of exfoliated lepidocrocite-type titanium oxide nanosheets (LTO) with alternating carbon layers via a solution-based self-assembly approach. Positively charged dopamine (Dopa) was used as the carbon precursor and intercalated between negatively charged exfoliated titania nanosheets through electrostatic interaction. Dopamine-intercalated LTO was then annealed under argon to form conductive carbon layers between titania sheets. The carbon content in the heterostructures was controlled by modifying self-assembly conditions (*i.e.* pH, stirring duration, and Dopa to LTO ratio). Electrodes were prepared using carbonized heterostructures (LTO-C) without adding more carbon to the composites and tested in sodium half-cell configurations. Higher capacities and improved capacity retention over 250 cycles, and lower impedance were observed as the carbon content of LTO-C heterostructures was increased from 0% (LTO nanosheets) to 30%. These results indicate that the self-assembly approach for 2D heterostructured electrode materials is a promising strategy to overcome electronic transport limitations of layered transition metal oxides and improve their electrochemical performance for next generation energy storage applications.

Keywords: Sodium-ion batteries, lepidocrocite titanate, anodes, dopamine, self-assembly

Introduction

Large-scale energy storage technologies are essential for mitigating the intermittency problems of renewable energy sources such as solar, wind, and waves. The development of sodium-ion batteries for large-scale grid storage applications has been driven by cost considerations and elemental abundance of sodium in the earth's crust. Performance improvements (*i.e.*, power density, energy density, lifetime) of sodium-ion batteries, however, require better electrode materials. The lack of suitable negative electrode

materials with high capacities and appropriate potentials is a major drawback for the development of sodium-ion batteries. Hard carbons are the most widely used Na^+ insertion anodes with their reasonably high capacities and good cycling behavior. However, their low densities impose an energy density penalty and the extremely low potentials close to the sodium plating potential at which sodium inserts into hard carbons give rise to some safety concerns.[1–4] Titanium-based layered transition metal oxides are denser and potentially safer alternatives to hard carbons and are reasonable in cost.[4–8] However, some intrinsic problems still exist. Oxides have a finite number of sites for ion insertion, which limits the Na^+ storage capacity, and thereby the achievable energy density. High power density requires fast ion and electron transport, but the transport of Na^+ in the commonly found corrugated layered metal oxides is sometimes restricted by structural considerations.[9] The poor electronic conductivity of the pristine materials is another impediment to the rate performance, and large amounts of carbon are frequently added to the composite electrodes to compensate.

Previously, our group reported on several Na^+ insertion anodes based on layered titanates showing high capacities (≥200 mAh g^{-1}) and low sodium intercalation potentials (~0.3 - 0.6 V *vs.* Na^+/Na).[10–13] Some of them are isostructural to the lepidocrocite mineral γ-FeOOH, which has a corrugated layered structure. Lepidocrocite-type titanates have the general formula of $A_xTi_{2-y}M_yO_4$, where A = K, Rb, or Cs, and M represents Li, Mg, Mn, Fe, Co, Ni, Cu, Zn or a vacancy.[9,14–16] Zigzag-type layered structures of lepidocrocite titanates consist of edge and corner-shared TiO_6 octahedra where A cations are located between the transition metal layers and M cations reside within layers. Recently, we have demonstrated sodium and lithium intercalation into lepidocrocite-type potassium titanate ($K_{0.8}Ti_{1.73}Li_{0.27}O_4$, KTL).[17] A theoretical capacity of 180 mAh g^{-1} was estimated based on site considerations. However, a low reversible specific capacity of 25 mAh g^{-1} upon sodium intercalation was observed, implying that only 15% of the available sites could be filled by sodium cations. Less site-limited versions were prepared by exchanging interlayer potassium ions with sodium. The sodium ion-exchanged form (*i.e.*, $Na_{0.8}Ti_{1.73}Li_{0.27}O_4$) delivered a higher reversible capacity of up to 140 mAh g^{-1} at a current density of 20 mA g^{-1}. If all the interlayer sites were available, the theoretical capacity for KTL would be 257 mAh g^{-1} based on full reduction of Ti^{4+} to Ti^{3+}. Recently, Yang *et al*. reported fast sodium intercalation into titania nanosheets by exfoliating KTL.[18] Exfoliated titania sheets were loosely restacked using various cations (*i.e.* Li^+, Na^+, K^+, Mg^{2+}). Upon Na^+-insertion into the Mg^{2+}-coagulated sample, a reversible capacity of 110 mAh g^{-1} was reported at a high current density of 3000 mA g^{-1}. The deviation of the practical capacity from the theoretical capacity was attributed to the Ohmic losses resulting from the low electronic conductivity of the coagulated titania sheets. A significant increase in the experimentally observed capacity (*i.e.*, 248 mAh g^{-1} at 20 mA g^{-1}) was reported upon increasing the amount of carbon additive from 20% to 40% in the composite electrodes.

An effective way to overcome the low electrical conductivity and slow ion transport of layered titanates is to manipulate the electrode structure. Heterostructures, assembled by stacking different layered materials (*e.g.*, transition metal oxides, carbides, nitrides, chalcogenides, graphene or reduced graphene oxides) can potentially overcome charge and ion transport issues. In these heterostructures, oxide layers alternate with conductive layers to make heterostructures with improved properties over the native oxides.[19,20] The 2D architectures of heterostructures provide larger ion diffusion channels for the facile transport of ions.[21,22] The increased interlayer distance of heterostructures can not only accommodate larger ions and/or enable their dense packing between the layers, but also reduces the ion diffusion energy barrier.[23–26] Zhao et al. recently reported a simple self-assembly strategy for the preparation of the van der Waals heterostructures of MoS_2 with N-doped graphene.[27] Exfoliated MoS_2 monolayers and dopamine molecules were self-assembled into dopamine-intercalated MoS_2, and in situ conversion of dopamine into nitrogen-doped graphene between MoS_2 layers resulted in the formation of heterostructures with well-defined alternating layers. In these heterostructures, the electronic conductivity and lithium-ion transport issues were alleviated by intercalating conductive components between exfoliated MoS_2 layers.

In this work, we demonstrate realization of this synthetic approach for oxide-based heterostructures for the first time. The lepidocrocite titanate-carbon nanosheets with well-defined alternating structures were prepared through self-assembly with dopamine. The carbon contents of the heterostructures were tuned by altering pH, self-assembly time, and dopamine amount. Chemical, structural and electrochemical characterization of the heterostructures was conducted, and composite electrodes were prepared without any carbon additives for electrochemical tests in sodium-ion half-cell configurations. Significant improvement in the electrochemical performance was observed as the carbon content of the heterostructures increased. Higher capacities and better capacity retention for materials with high carbon contents are associated with an increase in the electronic conductivity, which was further confirmed by electrochemical impedance spectroscopy.

Experimental

Materials: Titanium (IV) oxide, anatase (Sigma, 99.8%), potassium carbonate (Alfa Aesar, 99%), lithium carbonate (Alfa Aesar, 99%), tetramethylammonium hydroxide solution (Sigma, 25 wt% in H_2O), dopamine hydrochloride (Sigma), hydrochloric acid (Sigma, 37%).

Caution: Tetramethylammonium hydroxide is extremely toxic. We use appropriate personal protective equipment when handling, and avoid contact with skin.

Preparation of titania sheets: Potassium titanate ($K_{0.8}Ti_{1.73}Li_{0.27}O_4$) was synthesized via a solid-state method as previously described in the literature.[28] A stoichiometric mixture of TiO_2, K_2CO_3 and Li_2CO_3 was pressed into pellets and calcined at 900 ℃ for 20 hours (5 ℃/min). Exfoliation of the as-synthesized product was performed via a soft-chemical approach according to reference 29. $K_{0.8}Ti_{1.73}Li_{0.27}O_4$ was first protonated by stirring the powders in 1.0 M hydrochloric acid (HCl) solution for two days under ambient conditions (the solid-to-solution ratio was 10 g/L). The HCl solution was refreshed daily. The protonated product $H_{1.07}Ti_{1.73}O_4 \cdot H_2O$ was collected by filtration, washed with water, and air dried at room temperature. Protonated powder was stirred in tetramethylammonium hydroxide solution ($(CH_3)_4NOH$, TMA) for a week under ambient conditions to obtain monolayers. The concentration of TMA was adjusted to match the molar equivalence of exchangeable protons in the protonated product and the solid-to-solution ratio was 4 g/L. The exfoliated dispersion was centrifuged at 7500 rpm for 10 min to remove any unexfoliated material. The dispersion of the exfoliated sheets had a pH of 11.5. To remove the TMA ions, the monolayer dispersion was dialyzed with pure water until the pH was 7.

Preparation of heterostructures: The concentration of the titania sheets was adjusted to 0.5 mg/mL. A 5 molar excess of dopamine hydrochloride (Dopa-HCl) aqueous solution was prepared and added dropwise while stirring into the exfoliated titania sheets dispersion and further stirred at room temperature for either 5 or 60 minutes. At pH 7 the color of the dispersion turned to orange a few seconds after the addition of Dopa-HCl aqueous solution. At pH 11.5, black flocculates were observed after an hour stirring whereas flocculates remained orange for the mixture at pH 7. Flocculates were then collected by centrifuge at 10000 rpm for 10 min. The products were purified by washing with water and ethanol and then freeze dried. The dried products were annealed at 600 ℃ for 2 hours under argon to carbonize dopamine.

Preparation of Mg-coagulated titania sheets: Exfoliated titania sheets were coagulated with Mg^{2+} cations to form restacked LTO without carbon. Typically, 20 mL of 0.1 M $Mg(NO_3)_2$ solution was added into 20 mL of the titania dispersion (3.5 mg/mL) dropwise. The mixture was stirred overnight at RT and then freeze-dried.

Characterization: XRD data were collected on a Bruker D2 Phaser diffractometer with a CuKα source (λ = 1.5406 Å) equipped with a LynxEye detector, between 5 and 90° (2θ) at a rate of 0.0001°/s and a step size of 0.022°. Scanning Electron Microscopy (SEM) images were taken on a Phenom SEM equipped with a light optical camera with a magnification of 20-134x, and an electron optical magnification range of 200-1,000,000x equipped with an energy-dispersive x-ray spectrometer for mapping and elemental analysis. Thermogravimetric analysis (TGA) was carried out in air using a heating rate of 10 ℃/minute on a TA Instruments Q5500 TGA-MS instrument. Raman spectra were collected via a Horiba confocal Raman microscope with a 532 nm laser. Fourier Transform Infrared Spectroscopy (FT-IR) spectra were acquired with a Perkin Elmer Spectrum One FT-IR spectrometer from 600 to 4000 cm^{-1} in Attenuated-total-reflectance (ATR) mode. TEM imaging was conducted in a FEI ThemisX microscope with a high brightness xFEG field emission gun, operated at 300kV. Samples were dispersed in methanol and dropped onto a lacey carbon grid. For bright field TEM imaging, a Ceta camera was used, and an annular detector was used for dark field STEM imaging. EDS mapping for elemental analysis was conducted in STEM mode, using the ChemiSTEM detector, which captures X rays emitted in a solid angle of 0.9sr, significantly larger than typical X ray detectors.

The electrodes were cycled to a specific state of charge and disassembled in an argon-filled glovebox, and subsequently washed with dimethyl carbonate to remove salt residue. The dried and washed electrodes were sealed with kapton tape in an argon-filled glovebox and placed in aluminum pouches for transfer. Ex situ X-ray diffraction data was collected on beamline 11-3 at Stanford Synchrotron Radiation Lightsource (SSRL). The X-ray wavelength was calibrated to 0.9762 Å using a LaB_6 standard. Samples were packed between two pieces of Kapton tape. All hard X-ray Absorption Spectroscopy (XAS) measurements were carried out in transmission mode at beamline 4-3 at SSRL. Calibration was applied to all spectra using the first inflection point of the corresponding Ti metal foil. XAS data were analyzed using Athena software. Ex situ soft X-ray Absorption Spectroscopy (sXAS) data was collected on beamline 10-1 at room temperature under ultrahigh vacuum (10^{-9} Torr) using total electron yield (TEY). Samples for the ex-situ sXAS studies were prepared similarly to those for the hard XAS experiments. The cycled electrodes were mounted onto aluminum sample holders with double-sided carbon tape in an argon-filled glove box and transferred to the XAS load-lock chamber. All measurements were conducted using a 31-pole wiggler and a spherical grating monochromator with 20 mm entrance and exit slits, a 0.2 eV energy resolution and a 1 mm^2 beam spot.

X-ray Photoelectron Spectroscopy (XPS) was performed using a Thermo Scientific XPS instrument operating at a base pressure lower than 2×10^{-8} Torr, using an Al K-alpha source (λ = 1487 eV). Survey scans were acquired for all samples to identify possible presence of contaminants. A small amount of each powder was pressed against silver tape. This routinely guarantees good electrical contact and avoids charging as long as the starting material is conductive. High resolution spectra were acquired using a 50 meV pass energy over a measurement spot of 400 μm. Two different spots were measured for each sample with good reproducibility. Based on the inelastic mean free path determined reported for titanium compounds in reference 30, we approximate the probing depth of our measure to be 5-6 nm. Curve fitting was performed using Igor Pro software with a program coded as described in Ref 31. XPS peaks were fitted with a Gaussian-Lorentzian function. There was no need to change the ratio between the Gaussian and the Lorentzian so there was no distortion. Phase assignment was based on the characteristic binding energy separation that chemical species present as previously described.[29,30] All data are presented as acquired, without any rescaling with respect to binding energy (BE) axis.

The electrochemical properties of the compounds were evaluated in two-electrode 2032-coin cells containing metallic sodium as the counter electrode. Sodium disks were made by extruding dry sodium sticks (Sigma-Aldrich) into thin foils and cutting to size. Composite working electrodes were prepared by

making a slurry of 87.5 wt% of active material, and 12.5 wt% polyvinylidene difluoride (PVDF) (>99.5%, Aldrich) in N-methyl-2-pyrrolidinone (NMP) binder solution. No carbon was added to the slurries unless otherwise noted. The slurries were then cast onto carbon-coated aluminum foil. The electrodes were dried under vacuum at 120 ˚C for 12 h before being cut to size and weighed. The typical loading and thickness were ~ 1.0 – 1.5 mg cm^{-2} and ~ 150 μm, respectively. The electrolyte used for sodium cells was a solution of 1 M $NaPF_6$ (Alfa Aesar) in ethylene carbonate–diethylene carbonate (EC : DEC) 1 : 1 volume ratio mixed in-house. 0.5 M $NaBPh_4$ (sodium tetraphenylborate, Alfa Aesar) solution in diethylene glycol dimethyl ether (DEGDME) was also prepared and used as the electrolyte for some cells. Galvanostatic cycling experiments, cyclic voltammetry, and electrochemical impedance spectroscopy experiments were carried out using a BioLogic VMP3 potentiostat/galvanostat at room temperature. The cyclic voltammograms were obtained between 0.1−2.0 V with scan rates of 0.05-0.8 mV/s. The impedance spectra were recorded in the frequency range of 200 kHz to 1.4 mHz at a 10 mV amplitude after discharging to 0.1 V and charging to 2.0 V using a current density of 0.15 mA cm^{-2}. Cells were rested for half an hour after the galvanostatic experiments before impedance data were collected.

Results and Discussion

We used a self-assembly approach to prepare van der Waals heterostructures of lepidocrocite titanate with carbonized dopamine (**Scheme 1**). The parent lepidocrocite titanate ($K_{0.8}Ti_{1.73}Li_{0.27}O_4$, KTL) was prepared by solid-state synthesis as described in the Experimental Section. The C-base-centered orthorhombic structure of as-synthesized KTL with C*mcm* was confirmed by XRD, which agrees well with the previous reports (**Figure S1a**).[31,32] Pristine KTL was exfoliated by a two-step soft-chemical approach. In the first step, the protonated form was prepared by removing alkali metal cations (*i.e.,* potassium and lithium) via acid leaching.[18,33,34] Replacement of K between layers and Li in the titanate layers by protons leads to a swollen structure. The position of the lowest angle peak at 2θ=11.4° corresponding to the (020) plane in the XRD pattern shifts to the left after the material is protonated suggesting expansion of layers (**Figure S1a**). The protonated material retains its plate-like morphology with visible gaps between plates (**Figure S1b-c**). This material was then exfoliated in tetramethylammonium hydroxide solution via mechanical shaking. Exfoliated suspensions of titania sheets have a pH of 11.5 due to the presence of hydroxide ions. After dialysis against pure water, the pH dropped to 7.

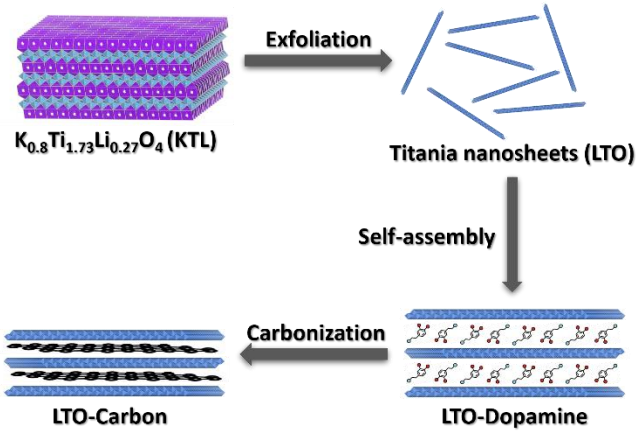

Scheme 1: Schematic illustration of the synthesis of lepidocrocite titanate-carbon heterostructures through self-assembly of exfoliated titania sheets and dopamine molecules followed by in situ carbonization via annealing.

The negatively charged titania sheets (LTO) self-assembled into heterostructures upon mixing with an aqueous solution of dopamine hydrochloride (Dopa) (**Scheme 1**). Dopamine attached onto surfaces of titania sheets through the positively charged ammonium groups during self-assembly. This process takes place immediately after the addition of the dopamine solution into the suspension of titanate sheets and continues until charge neutralization is complete, leading to the flocculation of LTO-Dopa heterostructures in the suspension (**Figure S2**). Self-assembly between titania sheets and dopamine was performed at pH 7 and pH 11.5 (*i.e.,* before and after dialysis of titania sheets) to monitor the impact of pH of the titania suspension on the charge neutralization (**Figure 1**). At pH 7, the color of the flocculate turned to orange, whereas at pH 11.5 the white titania suspension turned yellow, orange, and then greenish brown quickly in few minutes (**Figure S2**). After annealing under Ar, both orange and greenish brown LTO-Dopa powders turned completely black signifying carbonization of dopamine in the heterostructures.

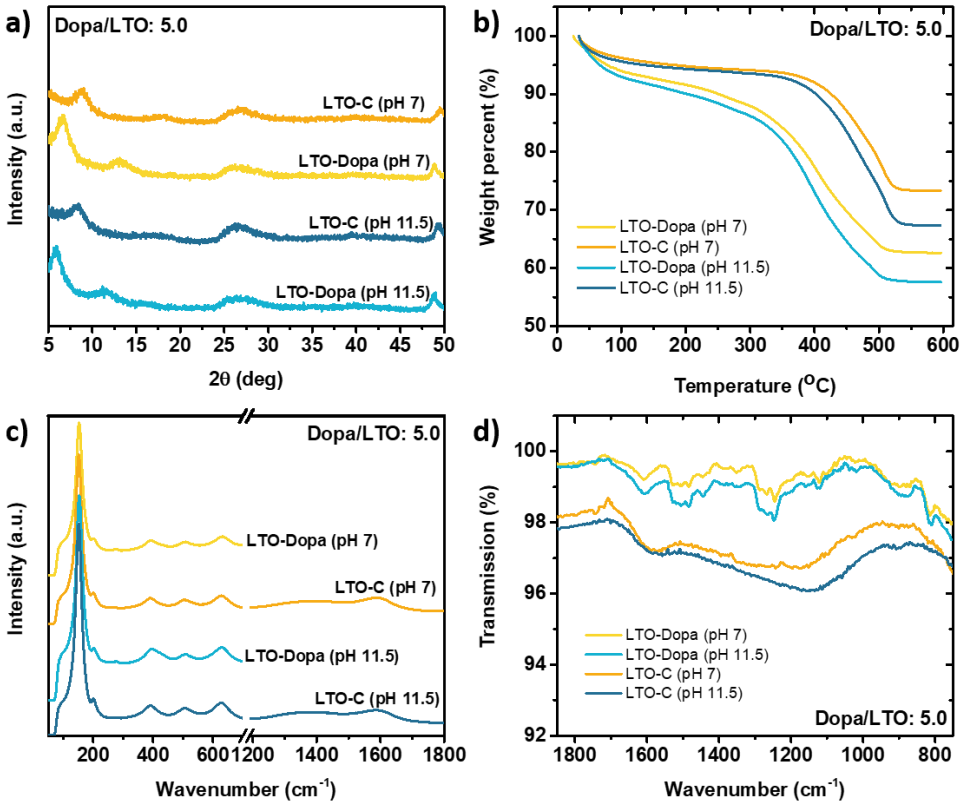

Figure 1: (a) XRD patterns, **(b)** TGA weight loss curves, **(c)** Raman spectra and **(d)** FT-IR spectra of lepidocrocite titanate – dopamine heterostructures before (LTO-Dopa) and after (LTO-C) carbonization at 600 ℃ for 2h under Argon.

Figure 1a shows XRD patterns of as-assembled heterostructures (LTO-Dopa) prepared under neutral and basic conditions after stirring for one hour and carbonized heterostructures (LTO-C), using an LTO/Dopa molar ratio of 5. The strong low angle broad peak in the patterns of the LTO-Dopa heterostructures prepared at pH 7 and pH 11.5, respectively, was observed at $2\theta = 6.6^{o}$ and 5.8^{o}, which corresponds to d-spacings of 1.33 nm and 1.52 nm. If the *Cmcm* symmetry of the original structure is maintained, this corresponds to half the *b*- lattice parameter (*i.e.,* it is the (020) reflection). The expansion

along the *b*-axis upon insertion of dopamine is 0.55 or 0.745 nm. These values are smaller than the length of the dopamine molecule (0.75 nm), suggesting tilting of the benzenediol tail, as was observed in $(DOPA)_xMoS_2$ due to interaction of the NH_3^+ groups with the MoS_2 monolayer.[27] After annealing at 600 ℃, the first peak shifts to higher angles (8.8° and 8.3°) for the pH 7 and pH 11.5 samples, indicating a decrease in the interlayer spacing to 1.00 nm and 1.06 nm, respectively (**Table S1**). The structures are still expanded compared to the parent compound, KTL, due to the presence of interlayer carbon.

TGA was used to determine the composition of the heterostructures. The weight loss up to 350 ℃ corresponds to the evaporation of physiosorbed water along with the removal of structural water. Between 350 and 550 ℃, the weight loss is associated with the removal of carbon from the heterostructures. The carbon content of the LTO-C heterostructure prepared at pH 7 is 20.5% whereas, it is 25.5% for the one prepared at pH 11.5, under otherwise identical conditions (**Figure 1b**). The higher carbon content of the heterostructure prepared at pH 11.5 suggests that charge neutralization between titania sheets and dopamine molecules is better facilitated under basic conditions and more dopamine molecules can be incorporated between titania sheets. The materials were further characterized by Raman spectroscopy to examine structural changes during carbonization. Similar Ti-O vibration bands below 750 cm^{-1} were observed for LTO-Dopa heterostructures prepared at pH 7 and pH 11.5 (**Figure 1c**). After calcination the bands remained the same, indicating that titania sheets do not restack and phase transformation to anatase TiO_2 does not take place during carbonization.[35,36] The two broad features at 1382 and 1586 cm^{-1} correspond to the D and G bands of carbon, respectively. The D:G ratios of 0.99 and 0.98 for LTO-C heterostructures prepared at pH 7 and pH 11.5 suggest that the carbon in LTO-C heterostructures is highly disordered.[37–39] Self-polymerization of dopamine under basic conditions has been reported previously.[40] FT-IR spectroscopy was used to examine oxidative polymerization of dopamine during self-assembly. Characteristic FT-IR bands of dopamine were observed between 750 and 1700 cm^{-1} consistent with C-N, O-H, C=O stretching and aromatic ring vibrations for both as-assembled LTO-Dopa heterostructures at pH 7 and pH 11.5 (**Figure 1d**). The lack of indole or indoline vibration bands around 1515 and 1605 cm^{-1} rules out oxidative self-polymerization of dopamine during self-assembly under both neutral and basic conditions.[41] After annealing, the FT-IR bands associated with the various functional groups are no longer observed.

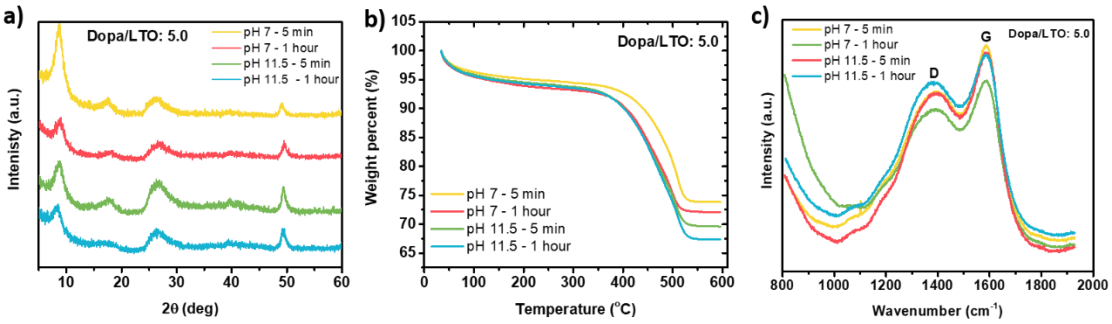

Figure 2: (a) XRD patterns, **(b)** TGA weight loss curves and **(c)** Raman spectra of heterostructures after carbonization at 600 ℃ for 2h under argon. Heterostructures were prepared by stirring for 5 min or an hour at pH 7 or pH 11.5.

To elucidate the effect of mixing time on self-assembly, LTO-C heterostructures were prepared from LTO-Dopa precursors stirred for either 5 min or an hour after the addition of dopamine solution into

the titanate suspension with a fixed Dopa:LTO molar ratio at 5.0. **Figure 2a** shows XRD patterns of the carbonized heterostructures prepared under neutral and basic conditions stirred either for 5 min or an hour. The first broad peak is located around 2θ~8.7° for both heterostructures prepared under neutral conditions or pH 11.5 and stirred for 5 minutes corresponding to a d-spacing of ~1.02 nm. The TGA analysis shows that the materials prepared under basic conditions stirred for either 5 minutes or one hour have carbon contents of 23.4 and 25.5% after calcination, respectively (**Figure 2b**). Lower carbon contents of 20% and 20.5% were calculated for heterostructures prepared at pH 7 stirred for 5 min and an hour, respectively. These results indicate that the carbon content of heterostructures can be tuned by changing the pH of the suspension but stirring time has a bigger effect at basic pH than neutral, probably due to faster kinetics at high pH. **Figure 2c** shows the Raman spectra of the LTO-C heterostructures with D and G bands of carbon indicated. A slight increase in the ratio of D to G band intensities from 0.98 to 0.99 was observed with the increasing self-assembly time from 5 min to an hour under both neutral and basic conditions. This suggests that incorporation of more carbon into heterostructures leads to more defect-rich carbon layers in the structure.[42]

After investigating the impact of pH and stirring time, we also carried out a series of experiments to gain insight on the effect of the Dopa:LTO molar ratio on the heterostructures. **Figure S3a** shows XRD patterns of carbonized heterostructures prepared with Dopa:LTO molar ratios of 0.66, 1.0 and 3.0 at pH 11.5 stirred for 5 min. Only one broad peak at ~8.5° was observed in the XRD pattern of the carbonized heterostructure with a Dopa:LTO molar ratio of 0.66. Heterostructures prepared with Dopa:LTO molar ratios of 1.0 and 3.0 have more intense low angle peaks at ~8.4° and ~8.3°, respectively with three other peaks at higher angles (**Figure S3a**). This difference in the diffraction patterns indicates that heterostructures prepared with Dopa:LTO molar ratios of 0.66 are less ordered than those made with larger amounts of dopamine. Furthermore, no flocculation was observed when we used a Dopa:LTO molar ratio of 0.5 or lower, implying that the amount of dopamine is not sufficient to complete charge neutralization. There was only a 2% increase in the carbon content when the Dopa:LTO molar ratio was increased from 0.66 to 3.0 for the materials prepared at pH 11.5, indicating that mainly electrostatic interactions between titania sheets and dopamine determine the maximum amount of dopamine that can be inserted (**Figure S3b**) and any excess is washed away during purification. Similarly, only a 3% decrease in the carbon content was found when the Dopa:LTO molar ratio was lowered from 5.0 to 1.0 for the heterostructures prepared at pH 7 with 5 min stirring (**Figure S4b**). The lowest carbon content was determined to be 17.5% for the carbonized heterostructure stirred for 5 minutes at pH 7 with a Dopa:LTO molar ratio of 1.0 (**Figure S4b**). After investigating the effects of pH, self-assembly time, and Dopa:LTO ratios, an LTO-C sample with 30% carbon content was also prepared using a Dopa:LTO ratio of 10.0 at pH 11.5 with an hour stirring (**Figure S5**). These results demonstrate that carbon content of heterostructures can be tuned from 17.5 to 30% by changing the pH of titania suspension, self-assembly time, and, in particular, Dopa:LTO molar ratios.

A summary of samples and their physical properties is presented in **Table S1**. Included in this table is the water content of samples determined by the weight loss below 400°C in the TGA experiments. This is considerably lower for LTO-C samples than for the LTO-Dopa materials, but varies randomly from about 5-10% with no clear relationship to physical characteristics such as carbon content. Most significantly, there is no correlation of water content with d-spacing or carbon content. Instead, the d-spacing increases in a roughly linear fashion with carbon content (Vegard's Law, **Figure S6a**). This is strong evidence that carbon is located in interlayer spaces, and that most of the water is physisorbed, rather than located between the titanate layers.

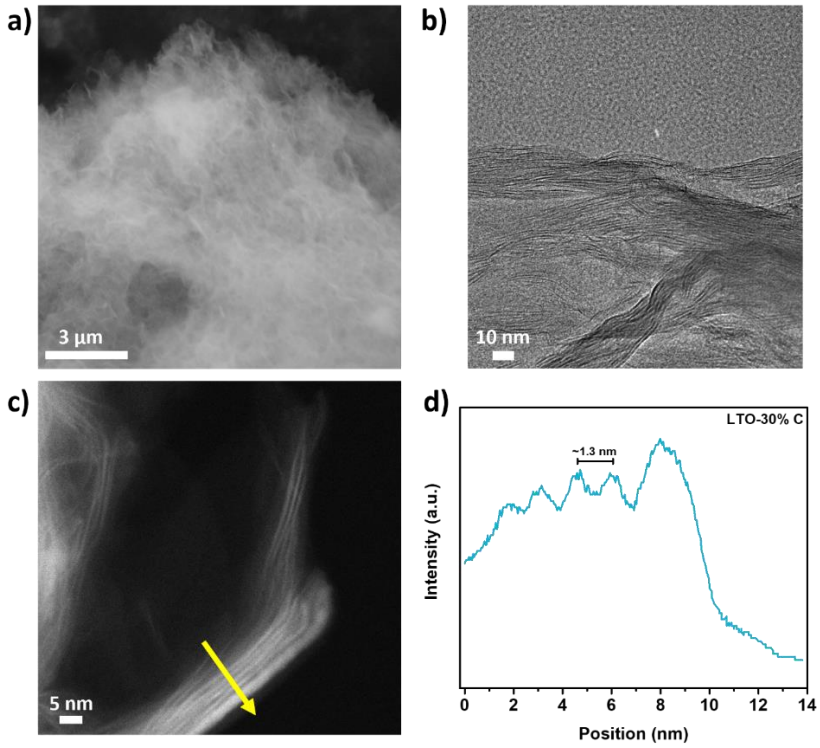

Figure 3: (a) SEM, **(b)** BFTEM and **(c)** HAADF micrographs of LTO-30%C heterostructure. **(d)** Average line histogram extracted by analyzing the region outlined by the yellow arrow in the HAADF image confirms a repeating layer spacing of ~1.3 nm.

The morphology of LTO-C heterostructures was characterized by electron microscopy. **Figure 3** displays SEM, BFTEM and HAADF images of the LTO-30%C heterostructure. Scanning electron microscopy (SEM) images show that this sample has a porous sheet-like morphology (**Figure 3a**). **Figures S7** and **S8** show SEM images of the LTO-30%C heterostructure at low and high magnifications along with elemental mapping. EDS mapping indicates that there is a homogenous distribution of Ti, C and O in the heterostructures at high magnifications, although a slightly higher C content was detected on the surfaces of particles at low magnifications. The carbon ratio was determined to be 28.6% in the low magnification images which agrees well with the TGA results. A higher carbon content (36%) was detected in the high magnification images, which map a single particle. Individual particles may vary in carbon content, although the overall average for this sample is roughly 30% as determined by TGA and EDS on the low magnification images. Free carbon was not detected in the low-resolution images. The Bright-field transmission electron microscopy (BFTEM) images further confirm the transparent sheet-like morphology indicating ultrathin sheets and layered morphology (**Figure 3b**). The high-angle annular dark-field (HAADF) images display the difference in the contrast between LTO and carbon layers (**Figure 3c**). Elemental composition of dark and bright regions in HAADF was analyzed by Energy-dispersive X-ray analysis (EDS). The darker areas exhibit higher carbon content and lower titanium content compared to the brighter areas verifying that there are alternating layers of LTO and carbon in the heterostructures (**Figure S9 and S10**). The spacing of ~1.3 nm between repeating layers were measured by line histograms extracted from the HAADF images (**Figure 3d**). This is somewhat larger than that found by XRD for this sample (1.16 nm). However, it is clear from the breadth of the low angle peak in the pattern that there is a distribution of d-spacings in this multi-particle sample.

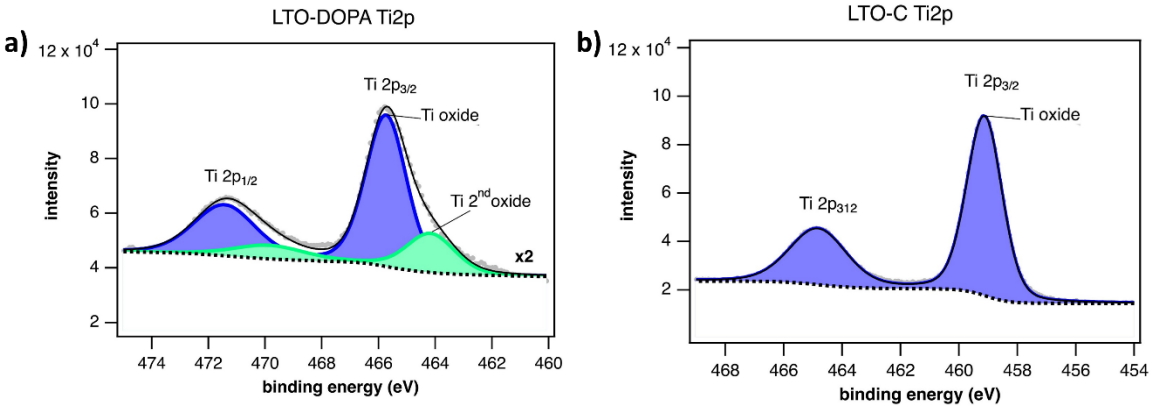

Figure 4: Ti 2p core level spectra showing two chemical environments for **(a)** LTO-DOPA sample and only one chemical environment for **(b)** LTO-23.4%C sample. Each chemical environment shows two peaks due to the spin orbit splitting. The spin orbit splitting for Ti peak is 5.7 eV which is typical for Ti in the +IV oxidation state for both lithium titanate and the suboxide.

XPS was performed to understand further the effect of the thermal treatment on the chemical and electronic properties of DOPA-lithium titanate powders. The thermally treated LTO-23.4%C sample showed good grounding, with the aliphatic components of the C1s core level spectroscopy located at 284.6 eV (**Figure S11f**). In contrast, the same components of the as-made LTO-DOPA heterostructure are located at 289.5 eV, substantially shifted to higher binding energies (**Figure S11e**). Large contributions from sp3 C-N configurations show the N-rich nature of the dopamine-derived carbon in thermally treated heterostructures. All peaks in the spectra of the LTO-DOPA heterostructures are broader than the peaks in the spectra of the LTO-C samples due to charging effects (**Figure S11**). This suggests that the thermal treatment reduces the intrinsic resistivity of the heterostructures. For battery materials, it is advisable to avoid the use of charge neutralization, as long as the charging effect is moderate and does not produce a distortion of the peaks, as in this case. This is because alkali metal cations are mobile and even the small charges produced by the neutralization process can induce a migration of the ions, to an extent that charge neutralizers are used to cycle battery materials during in-operando studies.[43] In cases like this, it is preferable to use the binding energy separation method, where the attribution of the given species is determined based on the characteristic separation between its two components.[29,30] The absolute position of the peaks can vary based on the position of the Fermi level in the material or because of charging, but the binding energy separation is a constant value unaffected by the above-mentioned processes. Therefore, all data are presented as acquired. Besides the improvement in electronic conductivity, the thermal treatment also changed the chemical environment of the titanium in the LTO-C heterostructures. In the LTO-DOPA heterostructures, there are two chemical environments for Ti present on the surface (**Figure 4a**). The first component is assigned to a stoichiometric form of lithium titanate, with a binding energy separation between the $Ti2p_{3/2}$ peak in the Ti core level spectrum and the O-Ti peak in the O core level spectrum equivalent to the values reported in reference samples (71.4 eV).[44] A second component (**Figure 4**), with a slightly lower binding energy separation (71.1 eV) is also present. The thermal treatment removes this second chemical environment completely (**Figure 4b**). The removal of this component is also observed in the oxygen core level spectrum (**Figure S11a,b**).

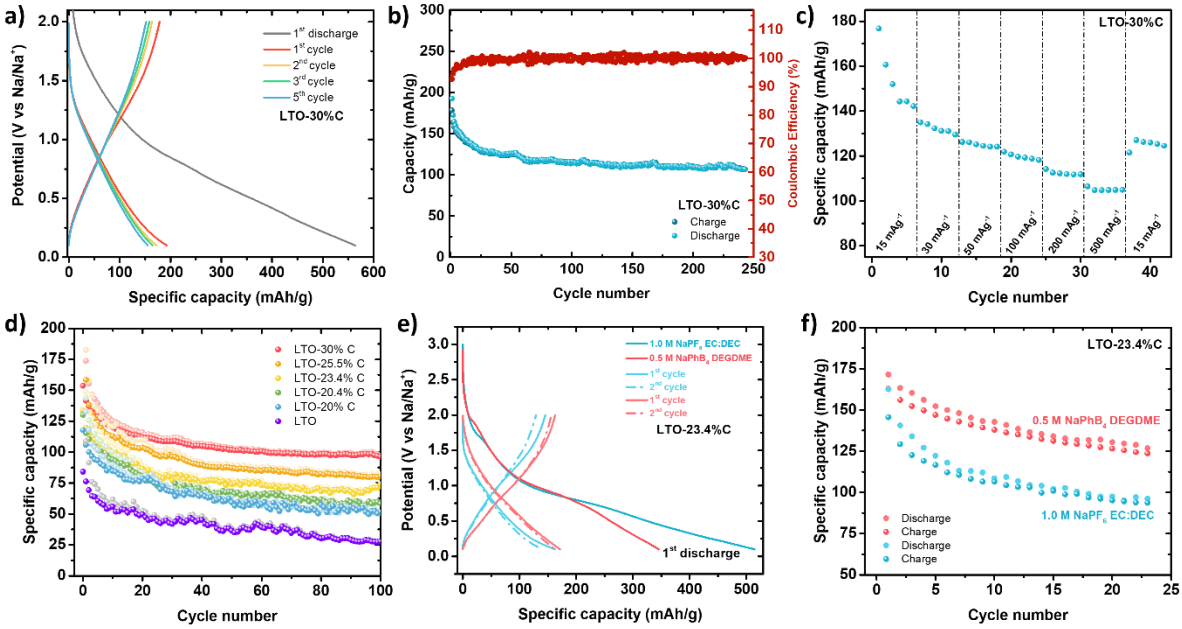

Figure 5: (a) Voltage profiles of sodium cells containing the LTO-30%C heterostructure for the first few cycles, **(b)** cycling performance at 15 mA g^{-1} (0.15 mA cm^{-2}) for 250 cycles, **(c)** rate performance, and **(d)** cycling performance at 15 mA g^{-1} of sodium cells containing LTO-C heterostructures as a function of carbon content for 100 cycles. First cycle capacities are omitted for clarity. Carbon content refers to the amount in the heterostructures; no additional carbon was included in the composite electrodes. One sample (LTO) made entirely without carbon consisted of exfoliated LTO sheets coagulated with Mg^{2+} cations. **(e)** Voltage profiles of sodium cells prepared with two different electrolytes and containing the LTO-23.4%C heterostructure during the first few cycles, **(f)** cycling performance at 15 mA g^{-1} (0.15 mA cm^{-2}) for 50 cycles using the indicated electrolytes.

The electrochemical performance of LTO-C heterostructures with various carbon contents were evaluated in 2032-type coin cells in a sodium half-cell configuration. Electrodes were prepared using the as-made heterostructures with a binder content of 12.5% and no additional carbon. **Figure 5a** shows the first few charge and discharge profiles of a cell containing the LTO-30%C heterostructure at a current density of 15 mA g^{-1} between 0.1V and 2.0V. This cell delivered an initial discharge capacity of 575 mAh g^{-1}, of which 178 mAh g^{-1} was recovered on the first charge. The low first cycle Coulombic efficiency can be attributed to side reactions at low potentials and formation of a solid-electrolyte interface. An average operating potential of 0.6 V *vs.* Na^+/Na was measured, similar to that of other lepidocrocite type sodium titanates, and lower than that of anatase TiO_2 (0.8 V *vs.* Na^+/Na).[9,13,17,45] **Figure 5b** displays capacity retention and Coulombic efficiency of the LTO-30%C heterostructure. The first cycle was removed for clarity. The second cycle Coulombic efficiency of 92% increased to 99% after ten cycles. On subsequent cycles, the Coulombic efficiency was over 99%, and the cell retained 56% of its second discharge capacity after 250 cycles (**Figure 5b**). The most significant loss was during the first 30 cycles corresponding to 34% of the second discharge capacity, after which the electrode exhibited improved capacity retention for more than 200 cycles suggesting good structural stability. The electrochemical performance of this cell was compared to those containing electrodes prepared with an additional 10% and 20% acetylene black. The electrode without any added acetylene black delivers a higher initial capacity than one containing 10%

acetylene black additive, suggesting that the conductivity of the LTO-C heterostructure was sufficient to overcome electronic transport issues in the electrode (**Figure S12**). Increasing the acetylene black content in the electrode to 20% did result in better capacity retention over 25 cycles, although the effect is modest. Rate capability results for cells containing the heterostructured LTO-30%C (no additional carbon in the electrodes) obtained with current densities ranging from 15 to 500 mA g^{-1} are presented in **Figure 5c**. A capacity close to what was obtained during the fifth cycle was recovered at the end of the test when the current density was reverted to 15 mA g^{-1}. The electrochemical performance of cells with LTO-C heterostructures containing various amounts of carbon but with no acetylene black added to the electrodes were also evaluated (**Figure 5d**). A cell containing an electrode prepared by coagulating titania sheets with Mg^{2+} (LTO) was also tested for comparison (*i.e.*, the active material was carbon-free as was the electrode). Interestingly, the initial capacities scale with the amount of carbon in the heterostructures, with the lowest value belonging to the completely carbon-free cell containing LTO nanosheets, clearly showing the advantages of this approach.

All the cells showed some evidence of capacity fading, but it mainly took place during the initial cycles, and stabilized after the first 30 cycles. To investigate the capacity fading during the first 30 cycles, SEM images (**Figure S13**) of pristine electrodes and those harvested from cycled cells show the formation of cracks and delamination from the current collector for an electrode cycled 31 times. The mechanical degradation is most likely the cause of the observed capacity fade. There is also an increase in the Na:Ti ratio for cycled electrodes, suggesting that some particles may have become disconnected after sodiation, and are no longer active. While the values of the initial capacities are similar for the cells containing heterostructures with carbon contents above 23.4%, the capacity retention is clearly best for the cell with LTO-30%C, which has the highest carbon content of all the heterostructures. Conversely, the poorest performance was observed for the cell with LTO nanosheets, which faded to 57% of the second discharge capacity after 10 cycles. Appropriate electrode engineering and judicious choice of electrolytic solution has been shown to improve the first cycle Coulombic efficiency in sodium half-cells.[13] To improve first cycle inefficiency and alleviate capacity fade in the first 30 cycles, we employed an ether-based electrolyte instead of a conventional carbonate-based electrolyte. A sodium cell containing the LTO-23.4%C heterostructure was prepared with 0.5 M $NaBPh_4$ in DEGDME and cycling performance compared with a cell containing 1.0 M $NaPF_6$ in ethylene carbonate–diethylene carbonate. A significant increase in the first cycle Coulombic efficiency from 28% to 47% was observed by changing the electrolyte to 0.5 M $NaBPh_4$/DEGDME from 1.0 M $NaPF_6$/EC:DEC (**Figure 5e**). Similarly, the retained first charge capacity increased to 163 mAh g^{-1} from 145 mAh g^{-1}. 74% of the second discharge capacity was retained after 22 cycles in the case of the cell with the ether-based electrolyte, whereas only 59% capacity retention was observed for the cell containing carbonate-based electrolyte (**Figure 5f**). These results imply that the ether-based electrolyte forms a more stable solid-electrolyte interphase and minimizes side-reactions. Additional cell-engineering is expected to further enhance electrochemical performance of the LTO-C heterostructures.

Cyclic voltammetry was carried out at different scan rates to gain further insight on the sodium insertion mechanism in LTO-C heterostructures. Cyclic voltammograms (CV) were recorded at various scan rates from 0.05 to 0.8 mV s^{-1}. The CV curves demonstrate a broad peak around 0.8 V and the nearly rectangular shape is suggestive of a pseudocapacitive mechanism (**Figure S14**). Kinetic analysis on the CV curves was conducted to assess the mechanism of Na^+ storage. The b value was estimated based on the relationship between peak current (i) and scan rate (ν): $i = a\nu^b$ where the b value indicates a diffusion-controlled intercalation ($b = 0.5$) or surface-controlled capacitive ($b = 1$) mechanism. A b value of 0.73 was determined by plotting $\log(i)$ versus $\log(\nu)$, suggesting a hybrid process involving both a slow diffusion-controlled process and a fast capacitive-like behavior. The contributions of the surface-controlled capacitive and diffusion-controlled mechanisms were quantified by separating the peak current (i) at a fixed voltage:

$i = k_1\nu + k_2\nu^{1/2}$. The contribution of the surface-controlled capacitive reaction was determined to be 24.5% at a scan rate of 0.05 mV s^{-1} indicating dominance of diffusion-controlled kinetics at slow scan rates (**Figure S14**). The contribution of the capacitive processes at other scan rates were also quantified. The contribution of surface-controlled capacitive process gradually increases to 56.5% as the scan rate rises to 0.8 mV s^{-1}.

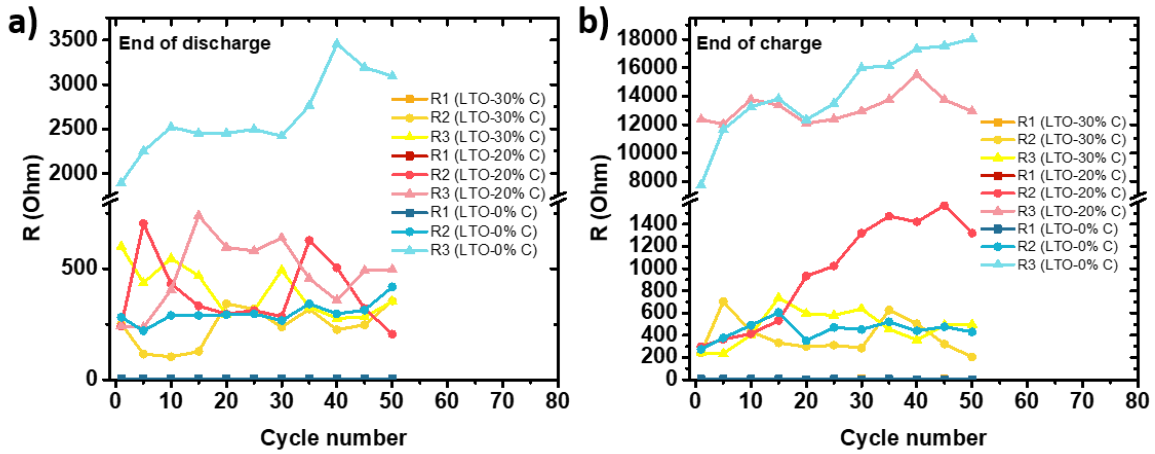

Figure 6: Resistivity values (R1, R2, R3) extracted from Nyquist plots of LT-C heterostructures in sodium half-cells after the end of the selected **(a)** discharge and **(b)** charge cycles. Cells were rested for half an hour before impedance data was collected.

Electrochemical impedance spectra (EIS) were recorded on cells before and after discharge over 50 cycles. EIS was applied to the cells after discharging to 0.1 V or charging to 2.0 V in the frequency range of 200 kHz to 1.4 mHz. Cells were rested for half an hour before collecting data. Nyquist plots of sodium half-cells containing LTO, LTO-20%C, or LTO-30%C heterostructures after selected discharge and charge cycles are shown in **Figure S15**. In most cases, two semi-circles are observed followed by a straight line at lower frequencies (Warburg diffusion). The smaller diameter of the semi-circle at high-to-midfield frequencies suggests better electronic conductivity in the composite electrode containing LTO-30%C compared to LTO-20%C and LTO-0%C. The data can be fit using an equivalent circuit model shown in **Figure S15g** with three components (R1, R2/Q2, and R3/Q3). R1 is related to the overall Ohmic resistance stemming from electrode, electrolyte, separator, and other cell components. By analogy to similar cells, the higher frequency semi-circle (R2/Q2) is associated with the sodium/electrolyte interface and SEI, and the lower frequency one (R3/Q3) with the properties of the composite electrode and its interface with the electrolyte. **Figure 6** display R1, R2, and R3 values of sodium half-cells with LTO-30%C, LTO-20%C, and LTO-0%C at the end of selected discharge and charge cycles. In all three cases, low R1 values were observed for cells compared to R2 and R3. R1 values of Na/LTO-30%C, Na/LTO-20%C and Na/LTO-0%C cells are comparable and remained constant during cycling.[11,17] R2 values are in roughly the same range for the three sets of cells and show somewhat random variation in a narrow range with cycling (although there is an anomalous increase with cycle number for the cell containing LTO-20%C at the end of charge, which is not observed at the end of discharge). The values of R3, in contrast, are highest for the LTO cell, and are markedly lower for those containing LTO-20% and LTO-30% at the end of discharge, implying higher charge transfer resistance for the former. Additionally, both Na/LTO-0%C and Na/LTO-20%C cells are significantly more resistive at the top of the charge than in the discharged state (**Figure S15**). The change in resistance for the Na/LTO-30%C cell between the discharged and charged states is

also much less pronounced than for the other two cells. This suggests that LTO-30%C is better able to compensate for lower intrinsic electronic conductivity of the titanates at the top of charge (**Figure 6b**).

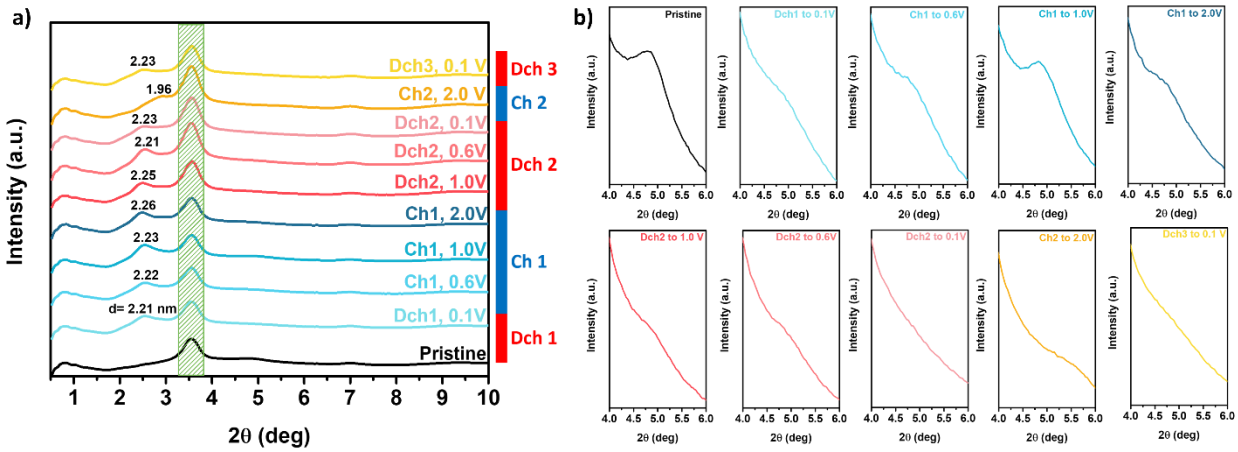

Figure 7: *Ex situ* synchrotron XRD patterns (λ = 0.9762 Å) of the LTO-23.4%C heterostructure at different states-of-charge after initial discharge to 0.1 V between **(a)** 2θ = 0.5 - 10°, **(b)** 2θ = 4 - 6°. The strong reflection at 2θ=3.5° (shaded) belongs to cell hardware. Blue indicates XRD patterns during the first charge from 0.1 V to 2.0 V. Red XRD patterns were collected during the subsequent discharge to 0.1 V, followed by charging to 2.0 V and a final discharge to 0.1V shown in yellow. Electrodes were cycled at a current density of 15 mA g^{-1}.

Ex situ synchrotron X-ray diffraction experiments were conducted to gain insights on the redox processes of LTO-C heterostructures upon sodium (de)insertion. **Figure 7a** displays XRD patterns of the LTO-23.4%C heterostructure at various states-of-charge. A prominent and invariant peak at 2θ = ~3.5° is associated with cell hardware. A weak shoulder near 2θ=5° in the pattern of the pristine (dry) electrode corresponds to a d-spacing of about 1.12 nm, somewhat larger than that found in the lab XRD experiment (**Figure 7b).** After the first discharge to 0.1 V, a new broad peak appeared at 2θ = ~2.5° corresponding to a d-spacing of 2.21 nm or nearly double that of the pristine material. This most likely indicates a change in symmetry, such as is seen when KTL is exchanged with sodium.[17] In that case, there is a shift of the corrugated titanate layers by *a*/2 with respect to one another, changing the cation coordination in the interlayer space from trigonal prismatic to cubic. The space group changes to *Pmmm*, and the lowest angle reflection is assigned to (010), with a d-spacing equivalent to the *b*-lattice parameter. In the case of the sodium-exchanged material, a weaker (020) reflection is also observed, and can also be observed here as a weak shoulder in the patterns of most of the electrodes near 2θ = ~5°. A leftward shift to 2θ = ~2.4° in the position of the low angle peak was observed as the cell was charged to 2.0 V indicating a further increase in d-spacing to 2.28 nm. The most significant shift was detected after the second charge to 2.0V. The lower angle peak shifts rightward to 2θ = ~2.88° demonstrating a decrease in the d-spacing to 1.93 nm. After the subsequent discharge to 0.1V, the peak shifted back to its initial position at 2θ = ~2.5°.

The breadths of the low angle reflections and considerable overlap with the adventitious peak near 2θ=3.5° make quantitative analysis of the results difficult. The large first cycle coulombic inefficiency also complicates the interpretation, since it is not possible to know the exact state-of-charge accurately. However,

it seems clear that sodium insertion into the heterostructure induces an irreversible structure change from C-type stacking to P-type. There is very little change in the *b*-lattice parameter upon initial sodiation and desodiation (approximately ±1-2%) but then there is a sharp contraction of about 12% upon the second charge, followed by an equally large expansion by the end of the third discharge, similar to what is found for the sodium-exchanged dehydrated version of KTL in sodium cells.[17] The larger than expected d-spacing in the pattern of the pristine material suggest that the heterostructure may have picked up water or solvent during processing into electrodes; the inserted sodium then displaces the neutral molecules located in the interlayer spacing, minimizing the initial change in the *b*-lattice parameter. The large lattice parameter change upon subsequent cycles may be responsible for the mechanical degradation and observed capacity loss; if so, this may be ameliorated through appropriate electrode engineering (*e.g.*, use of a more compliant binder).

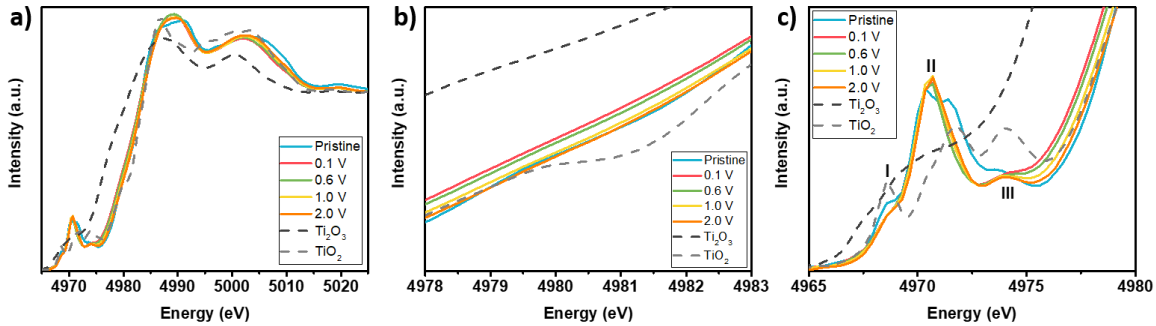

Figure 8: Ti K-edge XAS measurements of LTO-23.4%C electrodes at various states-of-charge **(a)** whole spectra, **(b)** edge region and **(c)** pre-edge region. Electrodes were cycled at a current density of 15 mA g^{-1}. XAS spectra of Ti_2O_3 and TiO_2 are also included as references.

Synchrotron XAS was conducted to gain insight on the electronic structure changes in the LTO-23.4%C heterostructure as a function of state-of-charge. Ti K-edge XAS probes the oxidation state in the bulk of the material. The peak position at 4948 eV for pristine LTO-23.4%C is consistent with a +4 oxidation state (compare to the spectrum of the TiO_2 reference material in **Figure 8**). For the electrodes partially or fully discharged, there is a progressive shift to lower energies, consistent with partial reduction to trivalent titanium. Upon recharge to 2.0V, there is a shift back to higher energy, close to the value found for the pristine material. However, the edge position of the most highly discharged electrode is still intermediate between those of TiO_2 and Ti_2O_3 reference materials, indicating that not all of the titanium is reduced (**Figure 8b**). The pre-edge region of XAS spectra yields information on metal coordination and chemical environment. The Ti pre-edge region consists of three peaks labelled I-II-III that are associated with the transition of 1s core electrons of Ti to the unoccupied hybridized states of Ti 3d–4s/4p (**Figure 8c**). Peak I and peak II are related to the t_{2g} bonding states and the nondirectional e_g antibonding states, respectively. The increased 4p-character of peak III can be ascribed to hybridization with Ti 4s and O 2p electrons.[46,47] The lower intensity of peak I in the case of cycled electrodes is also evidence of the partial reduction of Ti^{4+}. We used linear combination fitting to estimate the ratio of trivalent and tetravalent Ti in the electrodes as a function of state-of-charge (**Figure S16**). The second discharge capacity of 186 mAh g^{-1} for the LTO-23.4%C electrode suggests that 72% of the Ti should be reduced to the 3+ oxidation state upon sodium insertion if the mechanism is purely reductive intercalation. However, the XAS results indicate that only 32% of Ti is reduced after discharging to 0.1 V. (**Figure S16**). This discrepancy implies that some charge compensation occurs in the carbon and/or that the redox mechanism is partially capacitive. The coulombic inefficiency that is observed introduces uncertainty into these calculations, but the discrepancy is too large to discount these alternative mechanisms.

For the carbon-free LTO electrode, optical images of a discharged electrode show a dramatic change to dark blue from the original white of the pristine electrode (**Figure S17**). This is qualitative evidence of titanium reduction. Unfortunately, the black color of the pristine heterostructured electrodes does not allow a similar observation to be made.

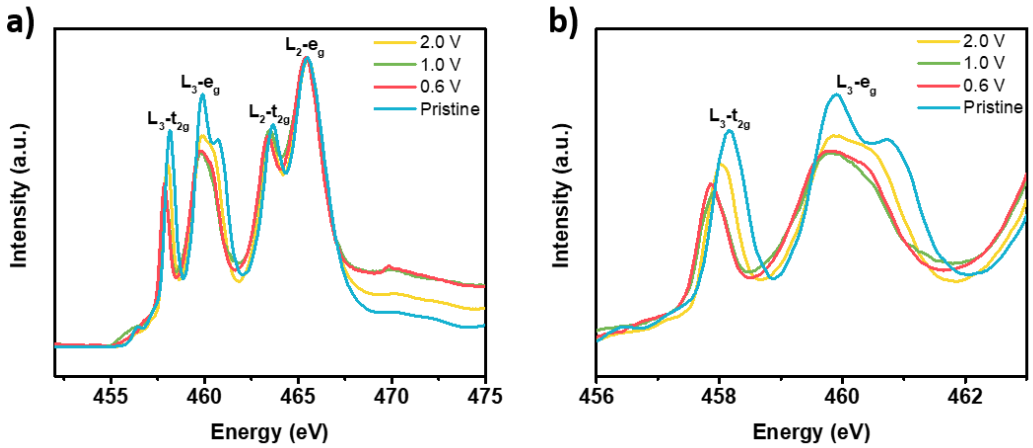

Figure 9: (a) Ti L-edge soft X-ray absorption measurements of LTO-23.4%C electrodes at various state-of-charge in the TEY mode and **(b)** Ti L_3-edge region. Electrodes were cycled at a current density of 15 mA g^{-1}.

Soft X-ray absorption measurements in total electron yield (TEY) mode were also conducted to probe the L-edge in the sub-surface regions (5-10 nm deep) of the heterostructures. Ti L-edge soft XAS yields information on the chemical environment of Ti atoms and surface groups owing to its high sensitivity to metal-ligand coordination. Soft XAS spectra of LTO-23.4%C electrodes at the Ti L-edge display four peaks (**Figure 9a**). L_3 and L_2-edge regions are the result of two-fold spin-orbit splitting of the Ti 2p levels into $2p_{1/2}$ (L_2) and $2p_{3/2}$ levels (L_3). The t_{2g} and e_g levels are associated with the two-fold splitting of 3d electron energies in the octahedral ligand field.[12,13,48,49] **Figure 9b** shows the Ti L_3-edge region of LTO-23.4%C electrodes at different state-of-charges. Both L_3-t_{2g} and peak L_3-t_{2g} positions shift towards lower energies as the electrode is discharged confirming that Ti is reduced.[50]

Conclusions

We have demonstrated synthesis of van der Waals heterostructures of exfoliated lepidocrocite-type titanium oxide nanosheets with carbonized dopamine (LTO-C) through a simple self-assembly approach. By changing experimental parameters, the carbon content can be tuned from 17.5 to 30% in the heterostructures. Incorporation of carbon nanosheets between titanate layers causes an expansion in the *b*-lattice parameter with the increase proportional to the amount of carbon in the heterostructure. TEM and HAADF analyses along with a linear increase in d-spacing with increasing carbon content confirm the presence of carbon nanosheets in the interlayer spaces. Carbon additive-free electrodes made from the heterostructures outperformed those containing titanium oxide nanosheets in sodium half cells, with the capacity and degree of capacity retention increasing with carbon content in the heterostructure. Best results were obtained for the LTO-30%C electrode material. The improvement was ascribed to the significantly lower impedance of this electrode observed in the EIS measurements, suggesting better electronic transport.

Ex situ XRD experiments show that insertion of sodium causes an irreversible structure change from a C-type lepidocrocite to a P-type and XAS results suggest that some charge compensation takes place on carbon rather than titanium and/or that the redox mechanism is partially capacitive.

Supporting Information

Additional XRD patterns and SEM images of pristine LTO and heterostructures; pictures of LTO-Dopa suspensions; HAADF micrographs, EDS and XPS analysis of heterostructures; electrochemical cycling, cyclic voltammogram and impedance data; linear combination fitting of XAS data

Acknowledgements

This work was supported as part of the Center for Mesoscale Transport Properties, an Energy Frontier Research Center supported by the U.S. Department of Energy, Office of Science, Basic Energy Sciences, under award #DE-SC0012673 including the following. Work at the Molecular Foundry of Lawrence Berkeley National Lab (LBNL) was supported by the Office of Science, Office of Basic Energy Sciences of the U.S. Department of Energy under Contract No. DE-AC02- 05CH11231. We would like to acknowledge the use of the Stanford Synchrotron Radiation Lightsource, SLAC National Accelerator Laboratory, that is supported by the U.S. Department of Energy, Office of Science, Office of Basic Energy Sciences under Contract No. DE-AC02-76SF00515. This document was prepared as an account of work sponsored by the United States Government. While this document is believed to contain correct information, neither the United States Government nor any agency thereof, nor the Regents of the University of California, nor any of their employees, makes any warranty, express or implied, or assumes any legal responsibility for the accuracy, completeness, or usefulness of any information, apparatus, product, or process disclosed, or represents that its use would not infringe privately owned rights. Reference herein to any specific commercial product, process, or service by its trade name, trademark, manufacturer, or otherwise, does not necessarily constitute or imply its endorsement, recommendation, or favoring by the United States Government or any agency thereof, or the Regents of the University of California. The views and opinions of authors expressed herein do not necessarily state or reject those of the United States Government or any agency thereof or the Regents of the University of California.

References

(1) Jensen, A. C. S.; Olsson, E.; Au, H.; Alptekin, H.; Yang, Z.; Cottrell, S.; Yokoyama, K.; Cai, Q.; Titirici, M.-M.; Drew, A. J. Local Mobility in Electrochemically Inactive Sodium in Hard Carbon Anodes after the First Cycle. *J. Mater. Chem. A* **2020**, *8* (2), 743–749.

(2) Liu, M.; Zhang, J.; Guo, S.; Wang, B.; Shen, Y.; Ai, X.; Yang, H.; Qian, J. Chemically Presodiated Hard Carbon Anodes with Enhanced Initial Coulombic Efficiencies for High-Energy Sodium Ion Batteries. *ACS Appl. Mater. Interfaces* **2020**, *12* (15), 17620–17627.

(3) Liu, X.; Jiang, X.; Zeng, Z.; Ai, X.; Yang, H.; Zhong, F.; Xia, Y.; Cao, Y. High Capacity and Cycle-Stable Hard Carbon Anode for Nonflammable Sodium-Ion Batteries. *ACS Appl. Mater. Interfaces* **2018**, *10* (44), 38141–38150.

(4) Pan, K.; Lu, H.; Zhong, F.; Ai, X.; Yang, H.; Cao, Y. Understanding the Electrochemical Compatibility and Reaction Mechanism on Na Metal and Hard Carbon Anodes of PC-Based Electrolytes for Sodium-Ion Batteries. *ACS Appl. Mater. Interfaces* **2018**, *10* (46), 39651–39660.

(5) Rudola, A.; Saravanan, K.; Mason, C. W.; Balaya, P. $Na_2Ti_3O_7$: An Intercalation Based Anode for Sodium-Ion Battery Applications. *J. Mater. Chem. A* **2013**, *1* (7), 2653.

(6) Sauvet, A.-L.; Baliteau, S.; Lopez, C.; Fabry, P. Synthesis and Characterization of Sodium Titanates $Na_2Ti_3O_7$ and $Na_2Ti_6O_{13}$. *J. Solid State Chem.* **2004**, *177* (12), 4508–4515.

(7) Ma, J.; Reeves, K. G.; Porras Gutierrez, A.-G.; Body, M.; Legein, C.; Kakinuma, K.; Borkiewicz, O. J.; Chapman, K. W.; Groult, H.; Salanne, M.; Dambournet, D. Layered Lepidocrocite Type Structure Isolated by Revisiting the Sol–Gel Chemistry of Anatase TiO_2: A New Anode Material for Batteries. *Chem. Mater.* **2017**, *29* (19), 8313–8324.

(8) Cech, O.; Castkova, K.; Chladil, L.; Dohnal, P.; Cudek, P.; Libich, J.; Vanysek, P. Synthesis and Characterization of $Na_2Ti_6O_{13}$ and $Na_2Ti_6O_{13}/Na_2Ti_3O_7$ Sodium Titanates with Nanorod-like Structure as Negative Electrode Materials for Sodium-Ion Batteries. *J. Energy Storage* **2017**, *14*, 391–398.

(9) Markus, I. M.; Engelke, S.; Shirpour, M.; Asta, M.; Doeff, M. Experimental and Computational Investigation of Lepidocrocite Anodes for Sodium-Ion Batteries. *Chem. Mater.* **2016**, *28* (12), 4284–4291.

(10) Doeff, M. M.; Cabana, J.; Shirpour, M. Titanate Anodes for Sodium Ion Batteries. *J. Inorg. Organomet. Polym. Mater.* **2014**, *24* (1), 5–14.

(11) Shirpour, M.; Cabana, J.; Doeff, M. New Materials Based on a Layered Sodium Titanate for Dual Electrochemical Na and Li Intercalation Systems. *Energy Environ. Sci.* **2013**, *6* (8), 2538.

(12) Alvarado, J.; Barim, G.; Quilty, C. D.; Yi, E.; Takeuchi, K. J.; Takeuchi, E. S.; Marschilok, A. C.; Doeff, M. M. Optimization of Nonatitanate Electrodes for Sodium-Ion Batteries. *J. Mater. Chem. A* **2020**, 10.1039.D0TA07561B.

(13) Yin, W.; Alvarado, J.; Barim, G.; Scott, M. C.; Peng, X.; Doeff, M. M. A Layered Nonstoichiometric Lepidocrocite-Type Sodium Titanate Anode Material for Sodium-Ion Batteries. *MRS Energy Sustain.* **2021**.

(14) Katogi, A.; Kubota, K.; Chihara, K.; Miyamoto, K.; Hasegawa, T.; Komaba, S. Synthesis and Electrochemical Performance of C-Base-Centered Lepidocrocite-like Titanates for Na-Ion Batteries. *ACS Appl. Energy Mater.* **2018**, *1* (8), 3630–3635.

(15) Gao, T.; Fjellvåg, H.; Norby, P. Protonic Titanate Derived from $Cs_xTi_{2-x/2}Mg_{x/2}O_4$ (x = 0.7) with Lepidocrocite-Type Layered Structure. *J Mater Chem* **2009**, *19* (6), 787–794.

(16) Reeves, K. G.; Ma, J.; Fukunishi, M.; Salanne, M.; Komaba, S.; Dambournet, D. Insights into Li^+, Na^+, and K^+ Intercalation in Lepidocrocite-Type Layered TiO_2 Structures. *ACS Appl. Energy Mater.* **2018**, *1* (5), 2078–2086.

(17) Shirpour, M.; Cabana, J.; Doeff, M. Lepidocrocite-Type Layered Titanate Structures: New Lithium and Sodium Ion Intercalation Anode Materials. *Chem. Mater.* **2014**, *26* (8), 2502–2512.

(18) Yang, J.; Xiao, X.; Gong, W.; Zhao, L.; Li, G.; Jiang, K.; Ma, R.; Rummeli, M. H.; Li, F.; Sasaki, T.; Geng, F. Size-Independent Fast Ion Intercalation in Two-Dimensional Titania Nanosheets for Alkali-Metal-Ion Batteries. *Angew. Chem. Int. Ed.* **2019**, *58* (26), 8740–8745.

(19) Das, P.; Fu, Q.; Bao, X.; Wu, Z.-S. Recent Advances in the Preparation, Characterization, and Applications of Two-Dimensional Heterostructures for Energy Storage and Conversion. *J. Mater. Chem. A* **2018**, *6* (44), 21747–21784.

(20) Geim, A. K.; Grigorieva, I. V. Van Der Waals Heterostructures. *Nature* **2013**, *499* (7459), 419–425.

(21) Xiong, P.; Ma, R.; Sakai, N.; Sasaki, T. Genuine Unilamellar Metal Oxide Nanosheets Confined in a Superlattice-like Structure for Superior Energy Storage. *ACS Nano* **2018**, *12* (2), 1768–1777.

(22) Xiong, P.; Zhang, F.; Zhang, X.; Wang, S.; Liu, H.; Sun, B.; Zhang, J.; Sun, Y.; Ma, R.; Bando, Y.; Zhou, C.; Liu, Z.; Sasaki, T.; Wang, G. Strain Engineering of Two-Dimensional Multilayered Heterostructures for beyond-Lithium-Based Rechargeable Batteries. *Nat. Commun.* **2020**, *11* (1), 3297.

(23) Deng, Y.; Wu, Z.; Liang, R.; Jiang, Y.; Luo, D.; Yu, A.; Chen, Z. Layer-Based Heterostructured Cathodes for Lithium-Ion and Sodium-Ion Batteries. *Adv. Funct. Mater.* **2019**, *29* (19), 1808522.

(24) Pomerantseva, E.; Gogotsi, Y. Two-Dimensional Heterostructures for Energy Storage. *Nat. Energy* **2017**, *2* (7), 17089.

(25) Xiong, P.; Wu, Y.; Liu, Y.; Ma, R.; Sasaki, T.; Wang, X.; Zhu, J. Two-Dimensional Organic–Inorganic Superlattice-like Heterostructures for Energy Storage Applications. *Energy Environ. Sci.* **2020**, *13* (12), 4834–4853.

(26) Zhu, Y.; Peng, W.; Li, Y.; Zhang, G.; Zhang, F.; Fan, X. Multiple Roles of a Heterointerface in Two-Dimensional van Der Waals Heterostructures: Insights into Energy-Related Applications. *J. Mater. Chem. A* **2019**, *7* (41), 23577–23603.
(27) Zhao, C.; Wang, X.; Kong, J.; Ang, J. M.; Lee, P. S.; Liu, Z.; Lu, X. Self-Assembly-Induced Alternately Stacked Single-Layer MoS_2 and N-Doped Graphene: A Novel van Der Waals Heterostructure for Lithium-Ion Batteries. *ACS Appl. Mater. Interfaces* **2016**, *8* (3), 2372–2379.
(28) Sasaki, T.; Kooli, F.; Iida, M.; Michiue, Y.; Takenouchi, S.; Yajima, Y.; Izumi, F.; Chakoumakos, B. C.; Watanabe, M. A Mixed Alkali Metal Titanate with the Lepidocrocite-like Layered Structure. Preparation, Crystal Structure, Protonic Form, and Acid−Base Intercalation Properties. *Chem. Mater.* **1998**, *10* (12), 4123–4128.
(29) Wood, K. N.; Teeter, G. XPS on Li-Battery-Related Compounds: Analysis of Inorganic SEI Phases and a Methodology for Charge Correction. *ACS Appl. Energy Mater.* **2018**, *1* (9), 4493–4504.
(30) Yin, Y.; Arca, E.; Wang, L.; Yang, G.; Schnabel, M.; Cao, L.; Xiao, C.; Zhou, H.; Liu, P.; Nanda, J.; Teeter, G.; Eichhorn, B.; Xu, K.; Burrell, A.; Ban, C. Nonpassivated Silicon Anode Surface. *ACS Appl. Mater. Interfaces* **2020**, *12* (23), 26593–26600.
(31) Tanaka, T.; Ebina, Y.; Takada, K.; Kurashima, K.; Sasaki, T. Oversized Titania Nanosheet Crystallites Derived from Flux-Grown Layered Titanate Single Crystals. *Chem. Mater.* **2003**, *15* (18), 3564–3568.
(32) Izumi, F.; Ikeda, T.; Sasaki, T.; Kumazawa, S. Disordered Distribution of K^+ Ions Interlayered in $K_xTi_{2-x/3}Li_{x/3}O_4$ (x = 0.8). *Mol. Cryst. Liq. Cryst. Sci. Technol. Sect. Mol. Cryst. Liq. Cryst.* **2000**, *341* (2), 253–258.
(33) Xiong, P.; Zhang, X.; Zhang, F.; Yi, D.; Zhang, J.; Sun, B.; Tian, H.; Shanmukaraj, D.; Rojo, T.; Armand, M.; Ma, R.; Sasaki, T.; Wang, G. Two-Dimensional Unilamellar Cation-Deficient Metal Oxide Nanosheet Superlattices for High-Rate Sodium Ion Energy Storage. *ACS Nano* **2018**, *12* (12), 12337–12346.
(34) Besselink, R.; Stawski, T. M.; Castricum, H. L.; Blank, D. H. A.; ten Elshof, J. E. Exfoliation and Restacking of Lepidocrocite-Type Layered Titanates Studied by Small-Angle X-Ray Scattering. *J. Phys. Chem. C* **2010**, *114* (49), 21281–21286.
(35) Fukuda, K.; Ebina, Y.; Shibata, T.; Aizawa, T.; Nakai, I.; Sasaki, T. Unusual Crystallization Behaviors of Anatase Nanocrystallites from a Molecularly Thin Titania Nanosheet and Its Stacked Forms: Increase in Nucleation Temperature and Oriented Growth. *J. Am. Chem. Soc.* **2007**, *129* (1), 202–209.
(36) Yuan, H.; Besselink, R.; Liao, Z.; ten Elshof, J. E. The Swelling Transition of Lepidocrocite-Type Protonated Layered Titanates into Anatase under Hydrothermal Treatment. *Sci. Rep.* **2015**, *4* (1), 4584.
(37) Zhu, L.; Yang, X.-X.; Xiang, Y.-H.; Kong, P.; Wu, X.-W. Neurons-System-like Structured SnS_2/CNTs Composite for High-Performance Sodium-Ion Battery Anode. *Rare Met.* **2021**, *40* (6), 1383–1390.
(38) Li, P.; Yang, Y.; Gong, S.; Lv, F.; Wang, W.; Li, Y.; Luo, M.; Xing, Y.; Wang, Q.; Guo, S. Co-Doped 1T-MoS_2 Nanosheets Embedded in N, S-Doped Carbon Nanobowls for High-Rate and Ultra-Stable Sodium-Ion Batteries. *Nano Res.* **2019**, *12* (9), 2218–2223.
(39) Su, D.; Huang, M.; Zhang, J.; Guo, X.; Chen, J.; Xue, Y.; Yuan, A.; Kong, Q. High N-Doped Hierarchical Porous Carbon Networks with Expanded Interlayers for Efficient Sodium Storage. *Nano Res.* **2020**, *13* (10), 2862–2868.
(40) Herlinger, E.; Jameson, R. F.; Linert, W. Spontaneous Autoxidation of Dopamine. *J. Chem. Soc. Perkin Trans. 2* **1995**, No. 2, 259.
(41) Dreyer, D. R.; Miller, D. J.; Freeman, B. D.; Paul, D. R.; Bielawski, C. W. Elucidating the Structure of Poly(Dopamine). *Langmuir* **2012**, *28* (15), 6428–6435.
(42) Clites, M.; Andris, R.; Cullen, D. A.; More, K. L.; Pomerantseva, E. Improving Electronic Conductivity of Layered Oxides through the Formation of Two-Dimensional Heterointerface for Intercalation Batteries. *ACS Appl. Energy Mater.* **2020**, *3* (4), 3835–3844.

(43) Wood, K. N.; Steirer, K. X.; Hafner, S. E.; Ban, C.; Santhanagopalan, S.; Lee, S.-H.; Teeter, G. Operando X-Ray Photoelectron Spectroscopy of Solid Electrolyte Interphase Formation and Evolution in Li_2S-P_2S_5 Solid-State Electrolytes. *Nat. Commun.* **2018**, *9* (1), 2490.
(44) Haasch, R. T.; Abraham, D. P. Lithium-Based Transition-Metal Oxides for Battery Electrodes Analyzed by x-Ray Photoelectron Spectroscopy. X. $Li_4Ti_5O_{12}$. *Surf. Sci. Spectra* **2019**, *26* (1), 014012.
(45) Tahir, M. N.; Oschmann, B.; Buchholz, D.; Dou, X.; Lieberwirth, I.; Panthöfer, M.; Tremel, W.; Zentel, R.; Passerini, S. Extraordinary Performance of Carbon-Coated Anatase TiO_2 as Sodium-Ion Anode. *Adv. Energy Mater.* **2016**, *6* (4), 1501489.
(46) Jiang, N.; Su, D.; Spence, J. C. H. Determination of Ti Coordination from Pre-Edge Peaks in Ti K -Edge XANES. *Phys. Rev. B* **2007**, *76* (21), 214117.
(47) Farges, F.; Brown, G. E.; Rehr, J. J. Ti K -Edge XANES Studies of Ti Coordination and Disorder in Oxide Compounds: Comparison between Theory and Experiment. *Phys. Rev. B* **1997**, *56* (4), 1809–1819.
(48) Ye, Y.; Kapilashrami, M.; Chuang, C.-H.; Liu, Y.; Glans, P.-A.; Guo, J. X-Ray Spectroscopies Studies of the 3d Transition Metal Oxides and Applications of Photocatalysis. *MRS Commun.* **2017**, *7* (1), 53–66.
(49) Guo, J. Interface Science in Nanoparticles: An Electronic Structure View of Photon-in/Photon-out Soft-X-Ray Spectroscopy: Interface Science in Nanoparticles. *Int. J. Quantum Chem.* **2009**, *109* (12), 2714–2721.
(50) Wang, T.-T.; Yang, Y.-T.; Lim, S.-C.; Chiang, C.-L.; Lim, J.-S.; Lin, Y.-C.; Peng, C.-K.; Lin, M.-C.; Lin, Y.-G. Hydrogenation Engineering of Bimetallic Ag–Cu-Modified-Titania Photocatalysts for Production of Hydrogen. *Catal. Today* **2020**, S0920586120307768.

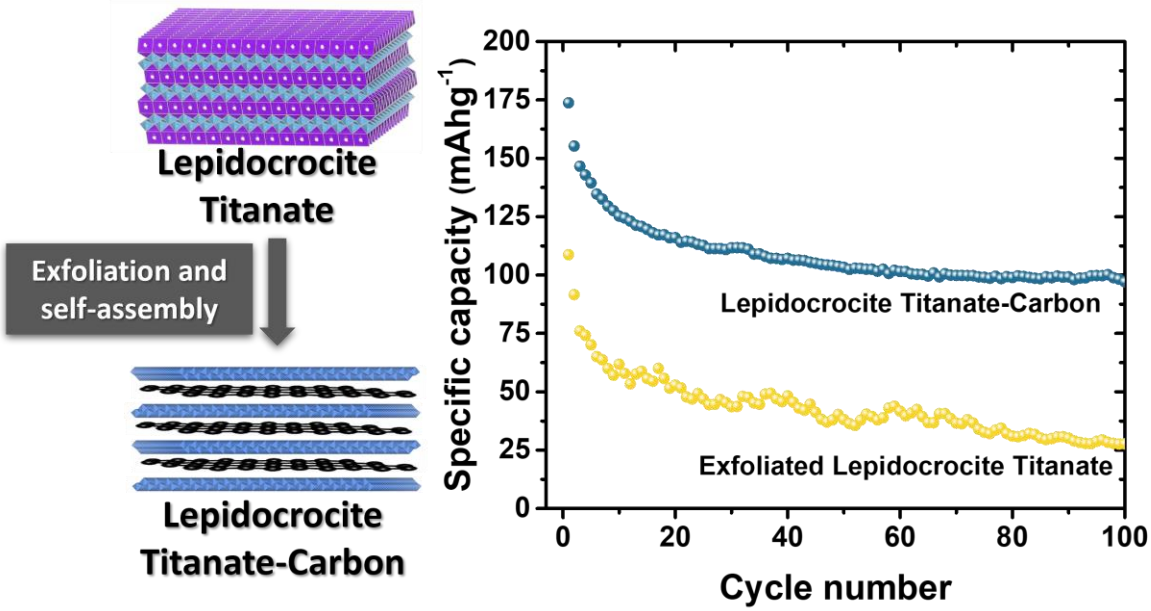
Lepidocrocite Titanate
Exfoliation and self-assembly
Lepidocrocite Titanate-Carbon
Specific capacity (mAhg-1)
Cycle number
Lepidocrocite Titanate-Carbon
Exfoliated Lepidocrocite Titanate
0
25
50
75
100
125
150
175
200
0
20
40
60
80
100